






RESEARCH ARTICLE | SEPTEMBER 21 2023

Multiscale computational framework to investigate integrin mechanosensing and cell adhesion

Andre R. Montes  ; Gabriela Gutierrez; Adrian Buganza Tepole   ; Mohammad R. K. Mofrad  

 Check for updates

J. Appl. Phys. 134, 114702 (2023)

<https://doi.org/10.1063/5.0164826>


View
Online


Export
Citation

CrossMark

Articles You May Be Interested In

A functional integral formalism for quantum spin systems

J. Math. Phys. (July 2008)

Modes selection in polymer mixtures undergoing phase separation by photochemical reactions

Chaos (June 1999)

Spreading of a surfactant monolayer on a thin liquid film: Onset and evolution of digitated structures

Chaos (March 1999)

500 kHz or 8.5 GHz?
And all the ranges in between.

Lock-in Amplifiers for your periodic signal measurements



Find out more

 Zurich
Instruments

Multiscale computational framework to investigate integrin mechanosensing and cell adhesion

Cite as: J. Appl. Phys. 134, 114702 (2023); doi: 10.1063/5.0164826

Submitted: 24 June 2023 · Accepted: 27 August 2023 ·

Published Online: 21 September 2023



Andre R. Montes,¹ Gabriela Gutierrez,¹ Adrian Buganza Tepole,^{2,a)} and Mohammad R. K. Mofrad^{1,a)}

AFFILIATIONS

¹Molecular Cell Biomechanics Laboratory, Departments of Bioengineering and Mechanical Engineering, University of California, Berkeley, California 94720, USA

²School of Mechanical Engineering, Purdue University, West Lafayette, Indiana 47907, USA and Molecular Biophysics and Integrative Bioimaging Division, Lawrence Berkeley National Lab, Berkeley, California 94720, USA

Note: This paper is part of the Special Topic on Multiscale Modeling and Analysis in Biophysics.

a) Authors to whom correspondence should be addressed: abuganza@purdue.edu. Tepole Mechanics and Mechanobiology Lab: engineering.purdue.edu/tepolelab/ mofrad@berkeley.edu. Molecular Cell Biomechanics Lab: biomechanics.berkeley.edu

ABSTRACT

Integrin mechanosensing plays an instrumental role in cell behavior, phenotype, and fate by transmitting mechanical signals that trigger downstream molecular and cellular changes. For instance, force transfer along key amino acid residues can mediate cell adhesion. Disrupting key binding sites within $\alpha_5\beta_1$ integrin's binding partner, fibronectin (FN) diminishes adhesive strength. While past studies have shown the importance of these residues in cell adhesion, the relationship between the dynamics of these residues and how integrin distributes force across the cell surface remains less explored. Here, we present a multiscale mechanical model to investigate the mechanical coupling between integrin nanoscale dynamics and whole-cell adhesion mechanics. Our framework leverages molecular dynamics simulations to investigate residues within $\alpha_5\beta_1$ -FN during stretching and the finite element method to visualize the whole-cell adhesion mechanics. The forces per integrin across the cell surface of the whole-cell model were consistent with past atomic force microscopy and Förster resonance energy transfer measurements from the literature. The molecular dynamics simulations also confirmed past studies that implicate two key sites within FN that maintain cell adhesion: the synergy site and arginine-glycine-aspartic acid (RGD) motif. Our study contributed to our understanding of molecular mechanisms by which these sites collaborate to mediate whole-cell integrin adhesion dynamics. Specifically, we showed how FN unfolding, residue binding/unbinding, and molecular structure contribute to $\alpha_5\beta_1$ -FN's nonlinear force-extension behavior during stretching. Our computational framework could be used to explain how the dynamics of key residues influence cell differentiation or how uniquely designed protein structures could dynamically limit the spread of metastatic cells.

Published under an exclusive license by AIP Publishing. <https://doi.org/10.1063/5.0164826>

I. INTRODUCTION

Cell-matrix junctions, governed in part by macromolecular structures known as focal adhesions (FAs), can alter cell phenotype, behavior, and fate via applied mechanical signals that trigger downstream molecular and cellular changes.^{1–9} At the heart of FA formation is a transmembrane heterodimer known as integrin containing α - and β -subunits. Normally, nascent FAs initiate with integrin activation, where cytoplasmic proteins bind to the integrin tails and the integrin head extends to an active state with a higher affinity for ligand binding.^{2,10} However, the activation of a

particular integrin, $\alpha_5\beta_1$, appears to follow a separate mechanism where an extended conformation may not be required to bind to its primary ligand, fibronectin (FN).^{11,12} Instead, $\alpha_5\beta_1$ binds to FN before cytoplasmic proteins anchor it to the cytoskeleton and additional integrins cluster together to create a mature FA [Fig. 1(a)].

The connection between $\alpha_5\beta_1$ integrin and FN is a main mechanosensing unit for external forces transmitting along amino acid residues that mediate cell adhesion.¹² The two principal $\alpha_5\beta_1$ binding sites in FN include the eight-amino-acid-long DRVPHSRN synergy site and the arginine-glycine-aspartic acid (RGD) motif.^{12–14}

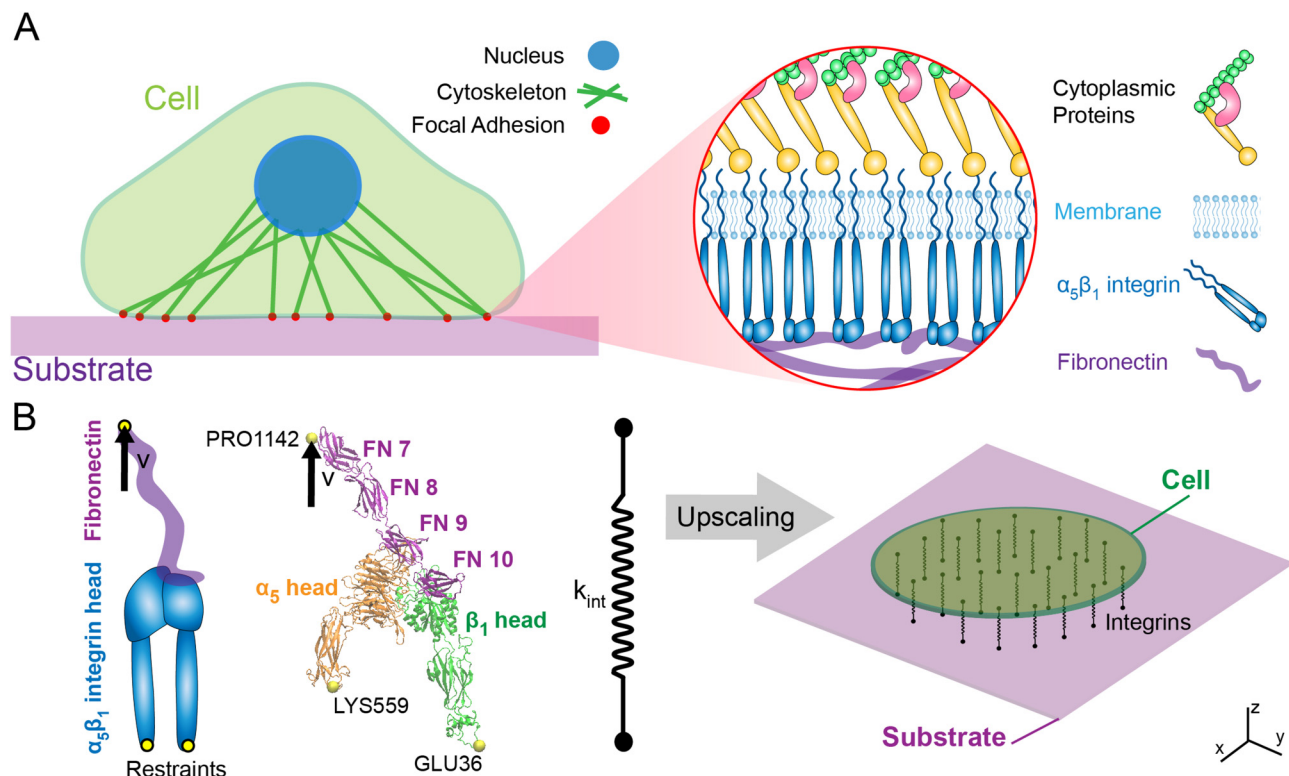


FIG. 1. Simplified schematic of multiscale cell mechanobiology within cell adhesion mediated by $\alpha_5\beta_1$ integrin. (a) The cell attaches to a substrate via FAs that house multiple biomolecules including cytoplasmic proteins that anchor integrins to corresponding ligands. (b) The molecular assembly consisted of $\alpha_5\beta_1$ integrin head bound to fibronectin type III fragment 7–10. For the MD simulations, restraints were placed on GLU36 and LYS559 with an applied velocity at PRO1142. The $\alpha_5\beta_1$ -FN's stretching behavior was characterized by a spring that was applied to a 2D continuum model of an elastic cell on a substrate.

21 September 2023 16:24:44

Upon mutation of R1374 and R1379 within the synergy site, spinning disk assays showed a reduction in cell-substrate adhesion strength; moreover, a perturbation of FN's RGD motif inhibited adhesion altogether.¹⁵ While the synergy site and RGD motif have been shown to play a role in cell adhesion, their nanoscale dynamics and force transduction pathway are less resolved. Elucidating how these residues maintain cell adhesion during integrin mechanosensing is important because their nanomechanics could be leveraged to control cell phenotype or motility.

Notably, $\alpha_5\beta_1$'s predominant role in mediating cell adhesion lends itself to be instrumental in the progression of various pathologies. For example, imposing a fibrotic microenvironment on cells by depositing collagen-I or applying biomechanical forces to the cancer cells leads to greater $\alpha_5\beta_1$ integrin-mediated proliferation.^{16,17} Similarly, as a tumor's rigidity increases, mechanosensitive $\alpha_5\beta_1$ integrins are recruited and cluster together, creating larger FAs and stress fibers that promote tumor growth via a positive biochemical and biophysical feedback loop.^{18,19} By understanding the link between nano- and micromechanics of the cell, we could influence differentiation or mitigate the uncontrolled spread of metastatic cells through targeted protein or drug design.

Therefore, to uncover the mechanical coupling between the nanoscale dynamics of key residues in $\alpha_5\beta_1$ integrin and whole-cell

adhesion dynamics, we built a multiscale model. Specifically, we combined adhesion kinetics, the finite element (FE) method, and molecular dynamics (MD) to demonstrate how key residues contributed to spring-like force-extension behavior, which, in turn, influenced the whole-cell spatial distribution of forces on integrins [Fig. 1(b)]. The force per integrin results from our model were within those measured by past atomic force microscopy (AFM)²⁰ and Förster resonance energy transfer (FRET) measurements.²¹ The model indicated localization of $\alpha_5\beta_1$ integrin along the cell periphery, which is consistent with cell-based studies that stain for β_1 integrin and FN fragments.²² Most importantly, the model contributed an inside look at the molecular dynamics by which the DRVPHSRN synergy site and RGD motif work together to mediate whole-cell adhesion mechanics.

II. METHODS

A. All-atom steered molecular dynamics

The 7NWL.pdb file containing human $\alpha_5\beta_1$ integrin in complex with FN and TS2/16 Fv-clasp was downloaded from the Protein Data Bank.¹² Schumacher *et al.* used the TS2/16 Fv-clasp to aid in the crystallization of $\alpha_5\beta_1$ -FN, and this was not naturally

occurring and was, therefore, removed using PyMOL 2.5,²³ leaving three protein chains to be analyzed as part of the remaining complex: α_5 integrin, β_1 integrin, and FN type III. We refer to this complex or system as “ $\alpha_5\beta_1$ -FN.”

All-atom molecular dynamics (MD) simulations were run in GROMACS 2018.3²⁴ with the AMBER99SB-ildn force field and periodic boundary conditions. Using the Gromacs built-in function, `gmx editconf`, we rotated the $\alpha_5\beta_1$ -FN complex 45° to align the structure inside a $18 \times 45 \times 19 \text{ nm}^3$ box. The structure was solvated in a TIP3P water box with 0.15 mM NaCl resulting in a system with 1.5×10^6 atoms.

The energy minimization step was carried out for 15 k steps utilizing the steepest gradient descent algorithm with a step size of 0.005 nm. Energy over time was extracted using the `gmx energy` command and then plotted in Python. The structure was then equilibrated using a sequential 1 ns NVT followed by a 10 ns NPT simulation with H-bonds restrained. For the NVT simulation, we used Nose–Hoover temperature coupling at 310 K. For the NPT simulation, Parrinello–Rahman pressure coupling at 1 bar was added. After the equilibration runs were completed, we extracted and plotted the root-mean-square deviation (RMSD), temperature, and pressure to confirm system stability.

Upon verifying system equilibration, we ran two steered MD simulations. The positions of Lysine (LYS) 559 and glutamic acid (GLU) 36 at the proximal ends of the integrin headpieces were restrained using the `gmx genrestr` command [Fig. 1(b)]. Proline (PRO) 1142 at the distal end of the FN chain was pulled vertically at 1 and 10 nm/ns using a 50 kJ/mol/nm spring with an umbrella potential for 25 and 3 ns, respectively. Constant force simulations were run with vertical pulling forces of 300 and 500 pN on PRO1142. The simulations only model the $\alpha_5\beta_1$ integrin headpiece and assume that the lower legs of $\alpha_5\beta_1$ and cell membrane, which are omitted, fix the positions of the headpieces at the proximal end. The model also assumes a completely vertical pulling load stemming from cell and substrate displacement and ignores any shear or rotational loads. The timestep for all steered MD simulations was 2 fs. The molecular dynamics parameter (.mdp) files for running the energy minimization, equilibration, and steered MD can be found in the supplementary material. We used the Gromacs built-in function `gmx gyrate` to measure the radius of gyration of the α_5 and β_1 integrin heads.

B. Force distribution analysis

Protein structures and MD simulation trajectories were visualized in Visual Molecular Dynamics (VMD) 1.9.4a.²⁵ We then used the Time-Resolved Force Distribution Analysis (FDA) software package, `gromacs-fda` (available: <https://github.com/HITS-MBM/gromacs-fda>) with Gromacs 2020.4 to calculate the punctual stresses at each of the residues along the α_5 and β_1 integrin chains, as well as FN. The punctual stress is the sum of absolute values of scalar pairwise forces exerted on each residue. The parameter settings for the FDA can be found in the supplementary material. The `gromacs-fda-vmd` plugin overlaid the punctual stress heatmap onto the protein renderings in VMD. Areas of interest for the FDA were the DRVPHSRN synergy site and RGD motif/loop (Fig. 2).

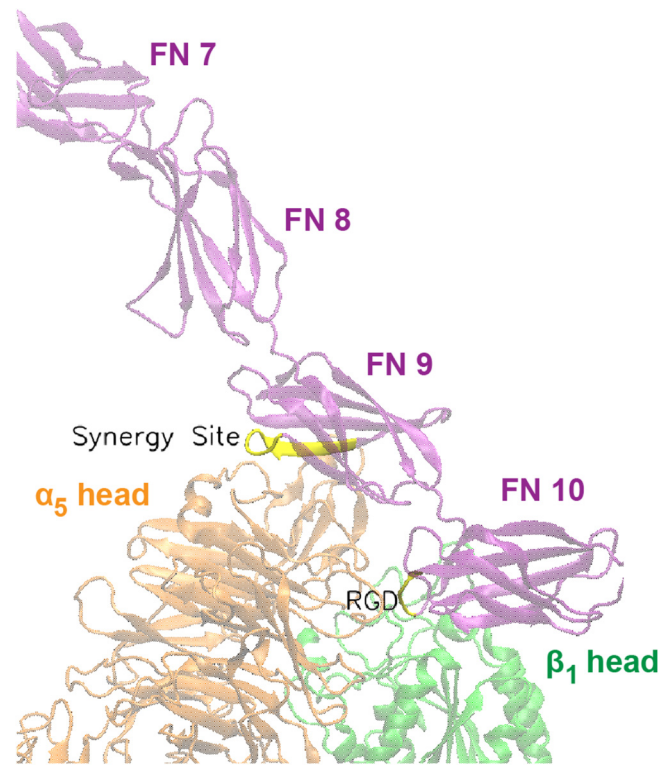


FIG. 2. Close-up view of DRVPHSRN synergy site and RGD motif/loop (shown in yellow) in FN that interact with the α_5 and β_1 heads, respectively.

21 September 2023 16:24:44

C. Whole-cell finite element model

The custom finite element (FE) model represented the cell as a thin elastic disk on top of an elastic substrate. The cell surface was assumed to be a neo-Hookean²⁶ constitutive material model,

$$\sigma_s^{\text{pas}} = \mu_s \mathbf{b}_s - p_s \mathbf{I}, \quad (1)$$

$$\sigma_c^{\text{pas}} = \mu_c \mathbf{b}_c - p_c \mathbf{I}, \quad (2)$$

where σ_s^{pas} and σ_c^{pas} are the passive substrate and cell stress, respectively. The shear moduli are denoted μ_s, μ_c (Table I). The deformation is characterized by the left Cauchy–Green tensors $\mathbf{b}_s, \mathbf{b}_c$. The pressures p_s, p_c are computed from boundary conditions, in this case for plane stress, ignoring 3D deformations.

To account for cell contractility, an active stress field was applied inside the cell,

$$\sigma_c^{\text{act}} = t_{\text{myo}} \mathbf{I}, \quad (3)$$

where σ_c^{act} is the active cell stress due to the applied actin-myosin traction, t_{myo} (Pa),

$$t_{\text{myo}} = \begin{cases} 100t, & 0 < t < 2, \\ 200, & 2 \leq t \leq 12, \end{cases} \quad (4)$$

TABLE I. Whole-cell model parameter settings.

Parameter	Variable	Setting
Substrate modulus	μ_s	1 MPa
Substrate density	ρ_s	$1.0 \mu\text{g}/\mu\text{m}^3$
Cell modulus	μ_c	1 kPa
Cell density	ρ_c	$1000 \text{ kg}/\text{m}^3$
Max $\alpha_5\beta_1$ -FN density	$\rho_{i,\text{max}}$	$100 \mu\text{m}^{-2}$
Catch-slip bond parameters	K_a	0.004 s^{-1}
	K_b	10 s^{-1}
	F_a	15 pN
	F_b	15 pN

where t is the simulation time. We used a previously developed catch-slip bond model of adhesion to determine the number of integrin-substrate bonds per node in the FE mesh in a force-dependent manner.^{27,28} This model assumes that the $\alpha_5\beta_1$ -FN complexes behave as parallel springs that connect and disconnect to the substrate based on an association constant, K_{on} and on a force-dependent dissociation constant, K_{off} , respectively,

$$K_{off} = K_a e^{\frac{f_{int}}{F_a}} + K_b e^{-\frac{f_{int}}{F_b}}, \quad (5)$$

where K_a , F_a , K_b , and F_b are fitted parameters (Table I) and f_{int} is the magnitude of the force per $\alpha_5\beta_1$ -FN bond. The force vector per bond, (\mathbf{f}_{int}), is computed via the $\alpha_5\beta_1$ -FN spring constant k_{int} and the spring extension vector \mathbf{u}_{int} ,

$$\mathbf{f}_{int} = k_{int} \mathbf{u}_{int}. \quad (6)$$

The force per node from integrin is related to the fraction (concentration) of $\alpha_5\beta_1$ -FN bonds C with respect to the maximum density $\rho_{i,\text{max}}$ (Table I), the local area of the adhesion A (area per node of the FE mesh), at that node,

$$\mathbf{f}_{i,node} = C \rho_{i,\text{max}} A \mathbf{f}_{int}. \quad (7)$$

The fraction of $\alpha_5\beta_1$ -FN bonds C needs to be updated in time. For a given node i and given the previous value of the bond concentration, C , the updated bond concentration $C_{t+\Delta t}$ at each subsequent time step is based on the update,

$$C_{t+\Delta t} = C(1 - K_{off}\Delta t) + K_{on}\Delta t(1 - C). \quad (8)$$

Note that the update Eq. (8) is based on treating the bond kinetics in the limit of an ordinary differential equation discretized in time with an explicit Euler scheme.

The internal force balance for the cell and substrate includes elastic deformation of the cell (σ_c^{pas}), active contractile stress within the cell (σ_c^{act}), and elastic deformation of the substrate (σ_s^{pas}),

$$\nabla \cdot \sigma_c = \rho_c \mathbf{a}_c, \quad (9)$$

$$\nabla \cdot \sigma_s = \rho_s \mathbf{a}_s, \quad (10)$$

where $\sigma_c = \sigma_c^{\text{pas}} + \sigma_c^{\text{act}}$ is the total stress in the cell, $\sigma_s = \sigma_s^{\text{pas}}$ is the total stress in the substrate, ρ_c, ρ_s are the densities of cell and substrate, respectively (Table I), and $\mathbf{a}_c, \mathbf{a}_s$ are the corresponding accelerations.

The strong forms of the elastodynamic equations (9) and (10) have boundary conditions of the form $\sigma \cdot \mathbf{n} = \mathbf{t}$ on boundary Γ . The strong forms are not directly evaluated. Rather, the internal forces were computed through the weak form. We multiplied both elastodynamic equations separately by test function, v , integrated over a domain Ω of thickness $1 \mu\text{m}$, and applied divergence theorem to get the following weak form for the cell (subscript c) and substrate (subscript s), respectively,

$$\begin{aligned} - \int_{\Omega_c} \sigma_c : \delta \mathbf{d}_c d\Omega_c + \int_{\Gamma_c} \mathbf{t}_c \cdot \delta v_c dA_c &= -\mathbf{R}_c + \mathbf{f}_{c,\text{ext}} \\ &= \int_{\Omega_c} \rho_c \mathbf{a}_c d\Omega_c, \end{aligned} \quad (11)$$

$$\begin{aligned} - \int_{\Omega_s} \sigma_s : \delta \mathbf{d}_s d\Omega_s + \int_{\Gamma_s} \mathbf{t}_s \cdot \delta v_s dA_s &= -\mathbf{R}_s + \mathbf{f}_{s,\text{ext}} \\ &= \int_{\Omega_s} \rho_s \mathbf{a}_s d\Omega_s, \end{aligned} \quad (12)$$

where δd is the variation of the symmetric velocity gradient, i.e., virtual work by moving each node by an independent variation δv . \mathbf{R} is the residual, and the external force acting at a particular node of the respective cell and substrate meshes is

$$\mathbf{f}_{c,\text{ext}} = \mathbf{f}_{i,node} + \mathbf{f}_d + \mathbf{f}_\kappa + \mathbf{f}_{ac} + \mathbf{f}_A, \quad (13)$$

$$\mathbf{f}_{s,\text{ext}} = -\mathbf{f}_{i,node} + \mathbf{f}_d, \quad (14)$$

where $\mathbf{f}_{i,node}$ is the force due to integrin at each node, \mathbf{f}_d is the viscous drag, \mathbf{f}_κ is the curvature regularization, \mathbf{f}_{ac} is a random fluctuation at the cell boundary from actin polymerization, and \mathbf{f}_A is an area penalty to counteract cell contractility. Note that the nodal integrin force acts on the cell and substrate surfaces in opposite directions. The remaining variables act on the cell border and are further explained in the supplementary material.

A dynamic explicit mesh generator, El Topo,²⁹ created and maintained the mesh during the simulation run. The explicit midpoint rule was used for time integration of the second order system of equations to update nodal velocities and positions. Three $\alpha_5\beta_1$ -FN stiffness values (k_{int}) were used: 1 pN/nm, 31 pN/nm, and variable stiffnesses extracted from the MD simulation force-extension curves (MD-driven). The variable stiffness of the $\alpha_5\beta_1$ -FN complex within the FE model was modeled as a nonlinear spring by applying piece-wise linear interpolation in Python to the force-extension curves provided by the MD simulations as described in Sec. II D. Settings for each simulation run can be found in the supplementary material.

The overall sequence of the multiscale model is summarized in Fig. 3. To summarize, the whole-cell FE model first imports the cell and substrate meshes and calculates the velocities and positions of the nodes. The $\alpha_5\beta_1$ -FN bonds are spread out uniformly across

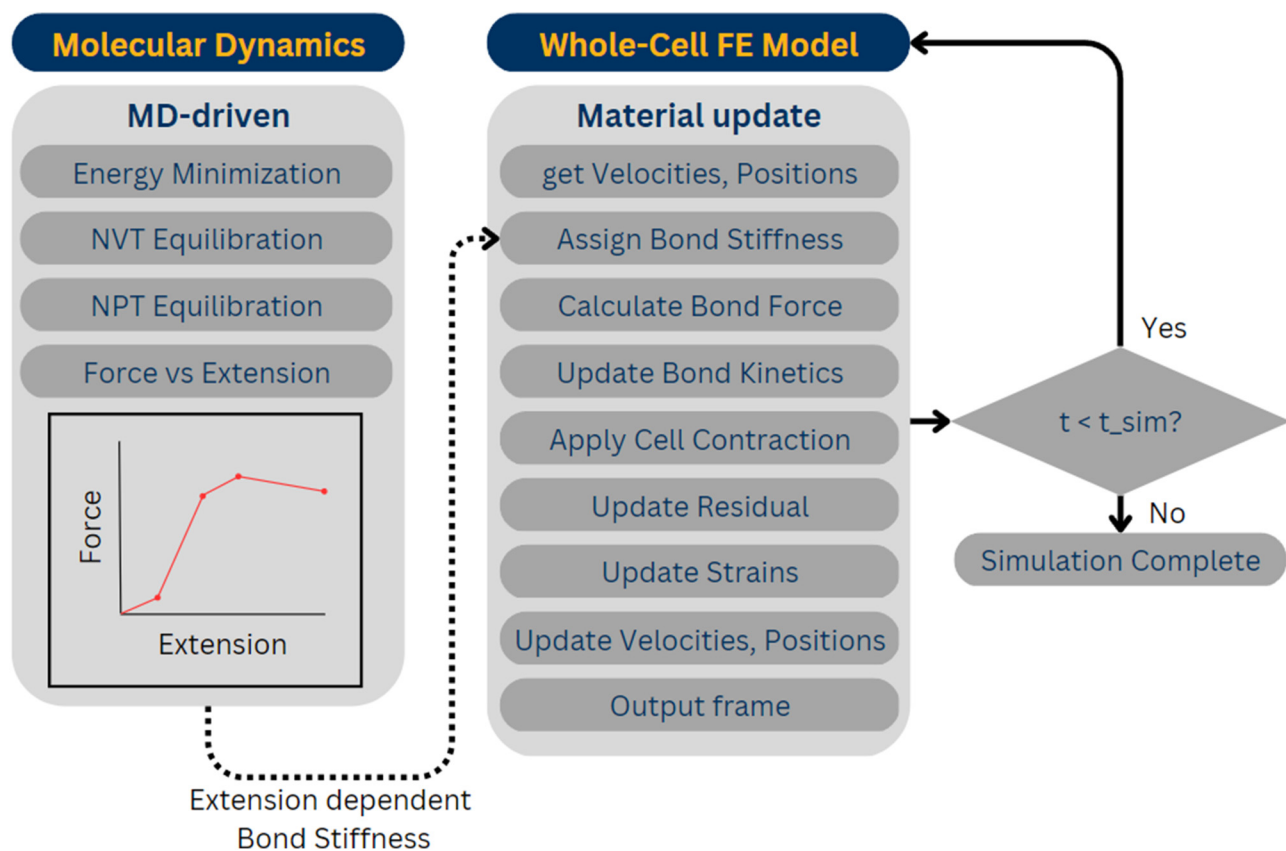


FIG. 3. Multiscale framework that links the MD model to the FE model via a variable spring constant.

the surface of the cell with bond attachment points on the cell and the substrate. The displacement between the cell and substrate attachment points dictates the bond stretch. For the MD-driven case, the bond stiffness, k_{int} , is assigned based on the bond stretch. Otherwise, the stiffness is directly assigned according to each constant case ($k_{int} = 1$ or 31 pN/nm). The force per bond is then calculated via Hooke's law [Eq. (6)]. This force is then used to update two things: the force per node [Eq. (7)] and the bond kinetics [Eqs. (5) and (8)]. Cell contraction [Eqs. (3) and (4)] is then applied and the residual is computed via the weak form [Eqs. (11) and (12)] considering the cell and substrate respective material properties [Eqs. (1) and (2)], their elastodynamics [Eqs. (9) and (10)], and their force balances [Eqs. (13) and (14)]. The nodal strains, velocities, and positions are updated and last, the simulation frame is saved. The whole-cell FE simulation iterates with a 1000-element mesh and a timestep of $dt = 50 \mu\text{s}$ over the course of an assigned time, $t_{sim} = 12$ s. Mesh and timestep convergence data can be found in the supplementary material.

D. Multiscale model coupling

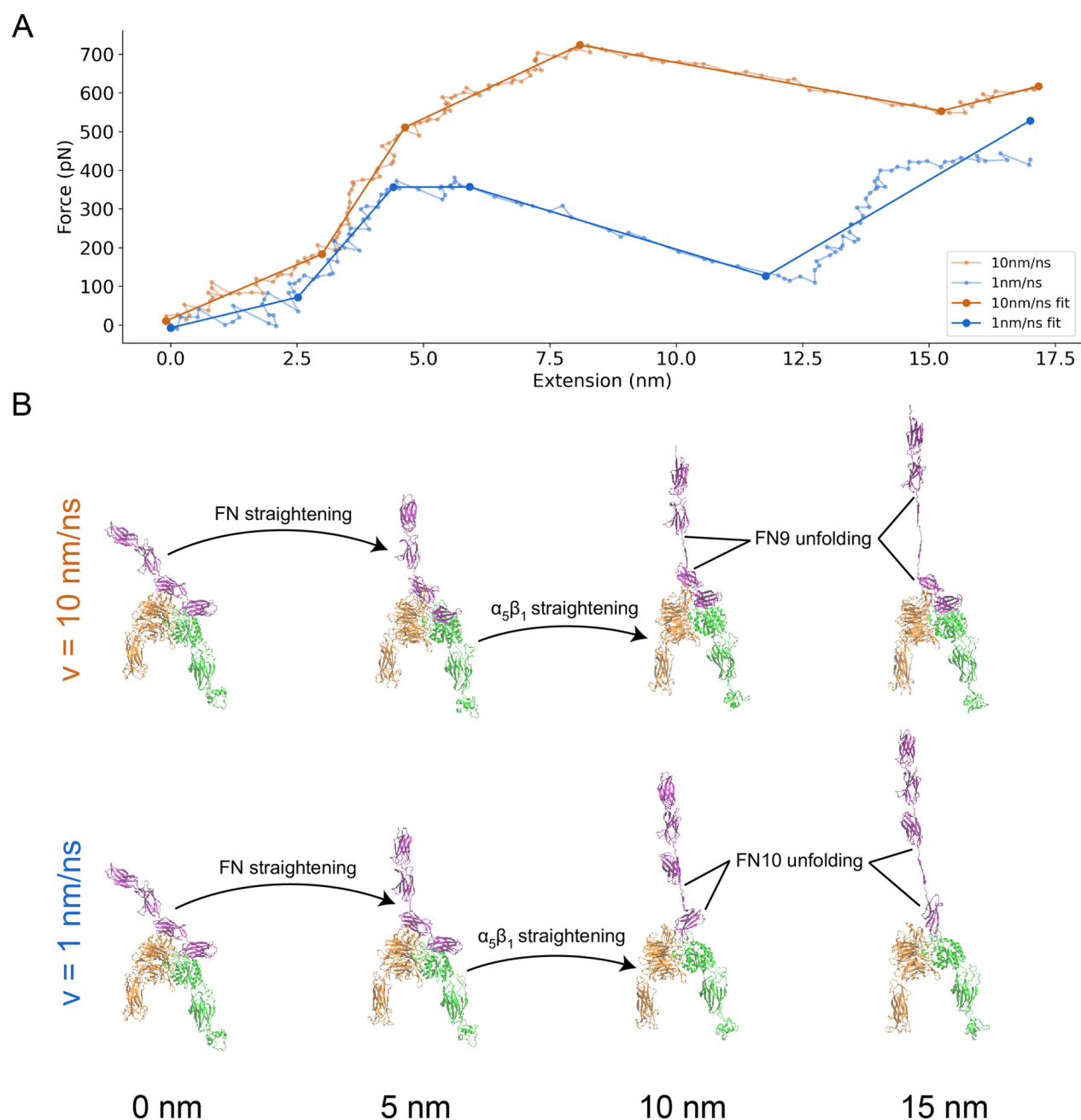
The Gromacs function, `mdrun`, output the force on the $\alpha_5\beta_1$ -FN complex. Furthermore, `gmx trajectory` was used to extract

the center-of-mass coordinates of the restraints, LYS559 and GLU36, as well as the pull residue, PRO1142. The $\alpha_5\beta_1$ -FN extension length was measured in Python as the average vertical distance between PRO1142 and each of the two restrained residues. The resulting force–extension curve for each simulation run was then plotted. The optimize function from the SciPy library was used to produce a five-segment piecewise linear fit on the 1 and 10 nm/ns force–extension curves, respectively. Ultimately, the 1 nm/ns curve fit was used as a variable displacement-dependent spring constant in the whole-cell model to make up the “MD-driven” $\alpha_5\beta_1$ -FN stiffness, k_{int} .

III. RESULTS AND DISCUSSION

A. $\alpha_5\beta_1$ -FN exhibited nonlinear and rate-dependent stretching behavior under applied constant velocity

Prior to running the steered MD simulations at two pulling rates, the model's energy minimized to $-1.37e7$ kJ/mol and the RMSD of the system plateaued while the pressure and temperature also remained stable during the NPT simulation (supplementary material). We chose 1 and 10 nm/ns pull rates for the steered MD simulations based on similar rates in other integrin subtypes.^{30,31} As expected, $\alpha_5\beta_1$ -FN exhibited rate-dependent stretching behavior, meaning that the $\alpha_5\beta_1$ -FN force–displacement curves varied by



21 September 2023 16:24:44

FIG. 4. (a) Force–extension curve of $\alpha_5\beta_1$ -FN stretching at 10 and 1 nm/ns. The raw data are shown in transparent solid lines and the five-segment piecewise linear fits are shown in opaque solid lines. (b) Frames of $\alpha_5\beta_1$ -FN during extension at 10 and 1 nm/ns showing distinct stretching configurations at 0, 5, 10, and 15 nm of extension. In both cases, FN and $\alpha_5\beta_1$ straightened before FN unfolded. However, for the 10 nm/ns case, the FN9 subdomain unfolded. Whereas for the 1 nm/ns case, FN10 unfolded. Movies showing $\alpha_5\beta_1$ -FN extension can be found in the supplementary material.

pull rate [Fig. 4(a)]. The 10 nm/ns simulation reached a higher peak force of 723 pN and greater initial slope of 56 pN/nm compared to 444 pN and 31 pN/nm, respectively, for the 1 nm/ns simulation.

In both cases, the stretching was dominated by FN, while integrin remained mostly rigid with some minor rotation and straightening. Curiously, at the faster 10 nm/ns pull rate, FN9 unraveled first before unbinding from the α_5 head at the synergy

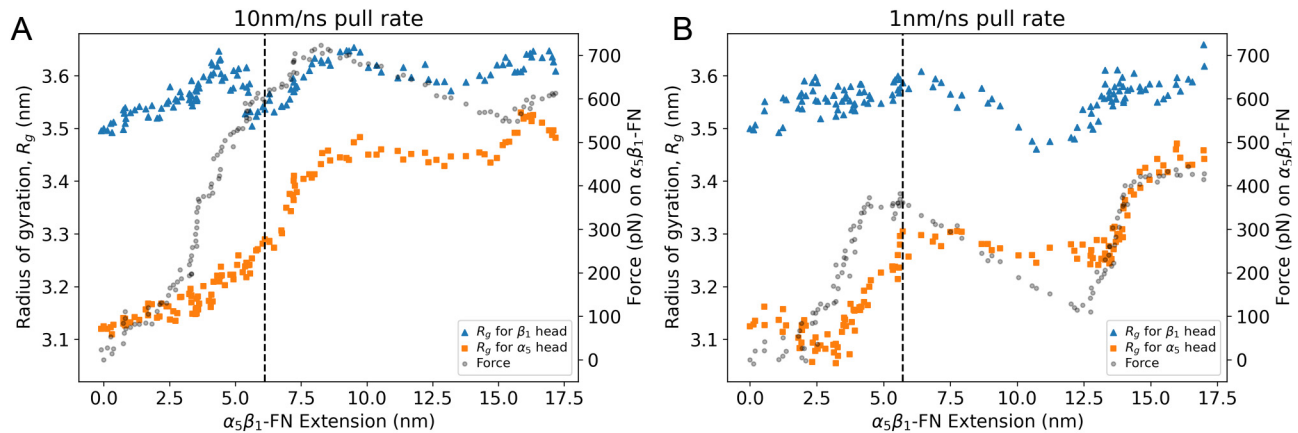


FIG. 5. Radius of gyration (left vertical axis) of α_5 and β_1 heads and force (right vertical axis) on $\alpha_5\beta_1$ -FN during (a) 10 and (b) 1 nm/ns extension. The dashed vertical line on each plot represents the moment the ARG1379-ASP154 salt bridge was broken.

site, whereas limited unraveling of FN was observed prior to unbinding for the slower 1 nm/ns pull rate [Fig. 4(b)]. Following the disconnection between FN and α_5 at the synergy site, the force on the whole $\alpha_5\beta_1$ integrin head became biased toward the RGD motif, causing the integrin heads to straighten with elongation of α_5 and β_1 . However, the degree of head straightening was not consistent for both pull rates over the course of $\alpha_5\beta_1$ -FN extension. We opted to use radius of gyration (R_g) as a proxy for integrin head straightness, with a larger radius indicating a straighter head. Visually, each integrin head started in a more closed position with a relatively small R_g before opening. Therefore, we believed it was appropriate to assume that a larger R_g corresponded to a straighter molecule. For both rates, we observed an initial increase in the R_g of both integrin heads prior to the unbinding of the salt bridge between arginine (ARG) 1379 in FN9 and aspartic acid (ASP) 154 in α_5 (Fig. 5). However, the faster rate showed a sharp increase in R_g of both heads after the salt bridge break at 6.1 nm, indicative of additional bonds pinning FN9 to α_5 that then led to FN9 unfolding and α_5 and β_1 head straightening. In contrast, at the slower rate, we noticed a steady decrease in R_g of both heads as FN10 unfolded immediately after the ARG1379-ASP154 break at 5.7 nm, presumably because α_5 was allowed to relax after the departure of FN9. The faster rate elicits a greater reaction force out of $\alpha_5\beta_1$ -FN, which were resisted by other bonds between FN9 and α_5 and a straightening of the integrin heads. This result was notable because it provided insight into how integrin may exhibit increased bond lifetime at higher forces, characteristic of previously observed catch bond behavior of integrins.^{15,32}

The observed viscoelastic behavior of $\alpha_5\beta_1$ has been shown both experimentally and computationally. Single-molecule AFM studies show higher rupture forces at faster pull rates²⁰ and separate steered MD simulations of integrin^{30,31} and FN³³ showed rate-dependent and force-dependent stretching behavior seen in viscoelastic materials. We expected this viscoelastic behavior to remain when $\alpha_5\beta_1$ and FN are *in silico* via constant force simulations at

300 and 500 pN, similar to what would be done in a mechanical creep test where constant stress is applied (Fig. 6). We fit the Bausch viscoelasticity model, which combines a Kelvin model with a dashpot in series,³⁴ to the extension–time plots, supporting the characterization of $\alpha_5\beta_1$ -FN's time-dependent stretching and viscoelastic nature.

While our MD simulations and previous literature have demonstrated the nonlinear stretching behavior of $\alpha_5\beta_1$ -FN, multiscale models assume a linear integrin stiffness between 0.001–2 pN/nm.^{27,28,35} Recent multiscale models have used this assumption when analyzing fundamental phenomena, such as integrin activation, organization, and clustering at the cell and tissue scales.^{27,28,35} Most recently, Guo *et al.* showed a framework that combined adhesion kinetics with the finite element method (FEM) to model stretch-driven mechanosensing at the tissue level by coupling

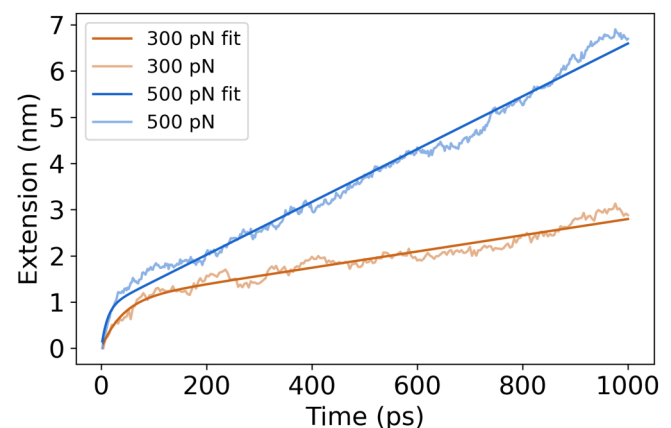


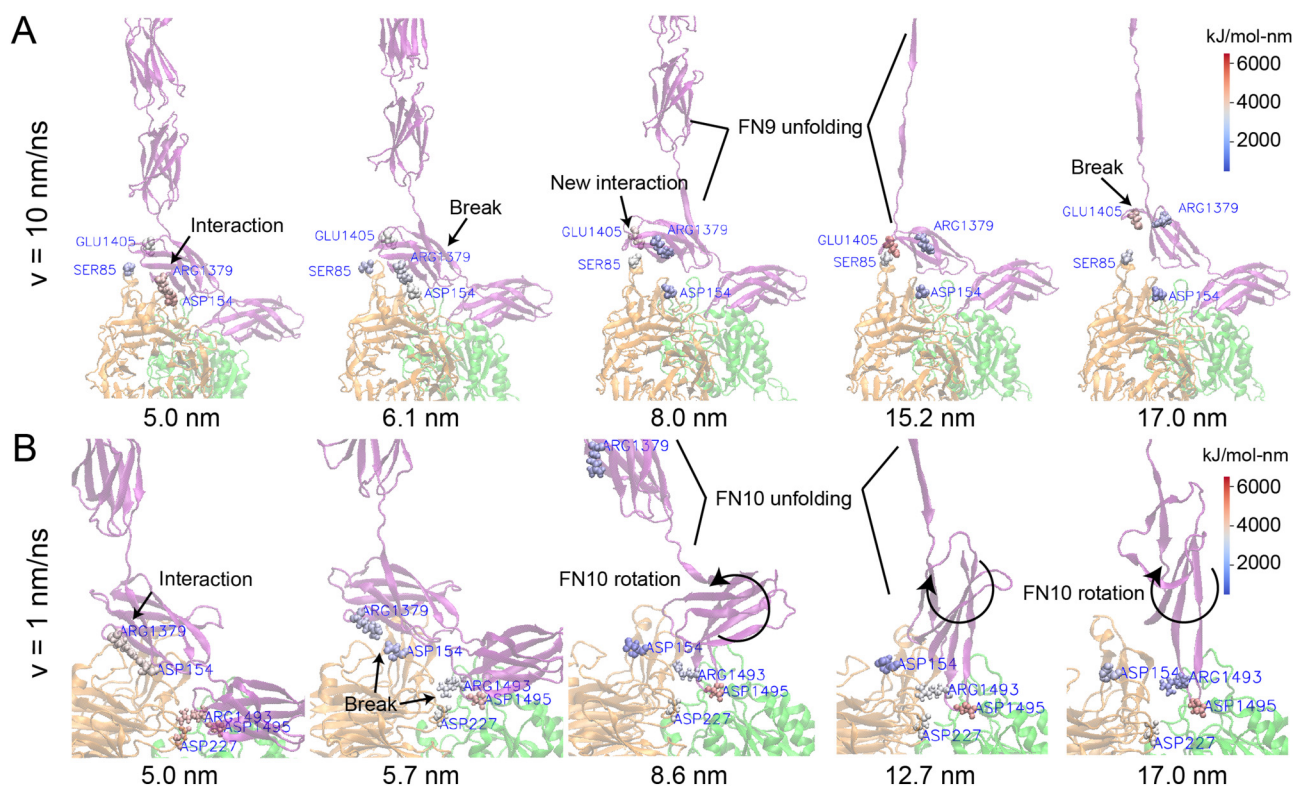
FIG. 6. Extension plots of constant force simulations at 300 and 500 pN pulling forces. The Bausch³⁴ viscoelastic model was fit to each of the plots.

21 September 2023 16:24:44

integrin adhesion with the nonlinear tissue mechanics of fibrin and collagen.²⁷ While these models provide unique insights into multi-scale mechanobiology of cell adhesion, for models to account for integrin and FN's nonlinear stretching behavior, a dynamic spring stiffness that adjusts depending on extension is required. For our work, we used our steered MD force–extension plots to inform a dynamically changing spring in a continuum model of the whole cell.

A limitation of our approach is that MD simulations are computationally expensive and runtimes would be unreasonably long if we adopted experimentally relevant 800 nm/s pull rates used by past AFM studies.^{36,37} However, using faster pull rates leads to higher single-molecule forces beyond 300pN as was noticed in our force–extension curves. Moreover, the MD model limited the flexibility of the proximal ends of the integrin heads by restraining them with a harmonic spring, potentially contributing to larger measured forces. The heads may have otherwise been more free to move depending on the motion of the integrin legs and tails within the cell membrane, which were not modeled to reduce

computational cost and add model stability. Previous studies found average *in situ* rupture forces for $\alpha_5\beta_1$ -FN to be 34³⁶ and 38.6 pN³⁷ in endothelial cells and cardiomyocytes, respectively. Single-molecule AFM conducted by Li *et al.* measured a mean rupture force of $\alpha_5\beta_1$ -FN of 69 pN at a loading rate of 1800–2000 pN/s, with a peak rupture force of 120 pN at 18 000 pN/s.²⁰ More recently, FRET-based sensors were used to measure adhesion forces between 1 and 7 pN on fibroblasts plated on glass.²¹ All these measured forces are much lower than those predicted by the MD simulations. Higher forces at much faster pull rates meant that our $\alpha_5\beta_1$ -FN stiffness results were significantly larger than what has been observed *in vitro*. However, in all the experiments, the nonlinearity of $\alpha_5\beta_1$ -FN's stretching behavior was apparent, challenging the linear stiffness assumption made by previous models.^{27,28,35} Furthermore, while an average FN stiffness of 0.5 pN/nm has been reported,^{38,39} the coupled $\alpha_5\beta_1$ -FN stiffness has not. Additionally, our steered MD simulations provided atomic level details that helped explain how key binding sites contributed to pull rate dependent nonlinear stretching.



21 September 2023 16:24:44

FIG. 7. Force distribution analysis of $\alpha_5\beta_1$ -FN for two pull rates at key events. The color map refers to the punctual stress (in kJ/mol-nm) at each residue. (a) At 10 nm/ns, there was a coulombic interaction at the ARG1379-ASP154 salt bridge and no interaction between GLU1405 and SER85. As FN was extended, the salt bridge ruptured and allowed FN to rotate and establish a new interaction between GLU1405 and SER85. FN continued to unfold, increasing stress on the GLU1405-SER85 connection, eventually breaking it. (b) At 1 nm/ns, the ARG1379-ASP154 salt bridge, part of the synergy site, together with ARG1493 and ARG1495, part of the RGD motif, maintained a hold on FN. As FN extended, increased stress led to the simultaneous rupture of ARG1493-ASP227 and ARG1379-ASP154. This allowed FN10 to unfold and rotate. ARG1493-ASP227 disconnected and reconnected throughout the remainder of the simulation. Movies showing the FDA can be found in the supplementary material.

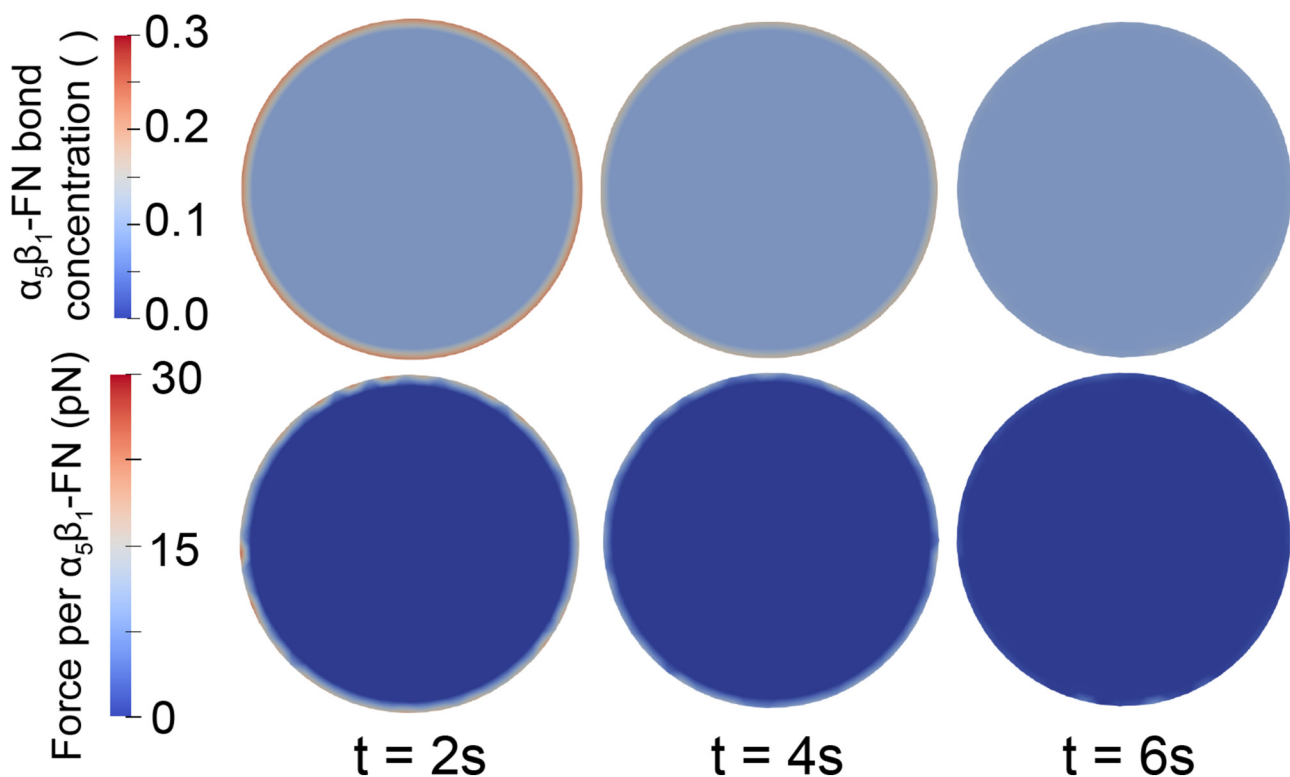
B. Force distribution analysis of $\alpha_5\beta_1$ -FN reveals dynamics of adhesion-mediating residues that contribute to nonlinear force–extension behavior

Visualization of the coulombic interactions via force distribution analysis of the steered MD results demonstrated how key adhesion mediators could contribute to nonlinear, rate-dependent, force–extension of $\alpha_5\beta_1$ -FN. Two key mediators are the DRVPHSRN synergy site and the RGD motif in FN (Fig. 2). In our system, the FN synergy site was represented by residues 1373–1380 and the RGD motif was represented by residues 1493–1495. Spinning disk microscopy has previously shown that mutating one to two select residues on the synergy site leads to a decrease in overall cell adhesion and mutating the RGD motif eliminates cell adhesion force completely.¹⁵ Furthermore, inducing a synergy site mutation or an RGD deletion leads to a reduction in single-molecule rupture force of $\alpha_5\beta_1$ -FN.²⁰ Therefore, we looked closely at the dynamics of these adhesion mediators during $\alpha_5\beta_1$ -FN stretching at 1 and 10 nm/ns.

Interestingly, the $\alpha_5\beta_1$ -FN extension showed two modes of stretching depending on the pull rate. Heatmaps overlaid on the molecule illustrated the degree of coulombic interaction, where “hotter” or “redder” zones indicated larger pairwise punctual stresses. For the 10 nm/ns case, the ARG1379-ASP154 salt bridge

is broken after 6.1 nm of $\alpha_5\beta_1$ -FN extension [Fig. 7(a)]. This action then loosens the grip between α_5 and FN9, allowing FN9 to rotate to find a new interaction between glutamic acid (GLU) 1405 and serine (SER) 85. FN9 then unfolded, contributing to the initial decrease in force and most of the extension before GLU1405 and SER85 release. Between 0 and 5 nm, FN began to straighten while simultaneously tugging on the synergy site and RGD. The force–extension response “softened” as the salt bridge was broken and FN9 started to rotate. The large extension and reduction in force past 8 nm (Fig. 4) was due to the rapid unfolding of FN9 while GLU1405-SER85 pinned the rest of FN9 in place. After two strands of FN9 are unwound, the applied load became directed at the GLU1405-SER85 pin until it finally separated. Notably, the unfolding pathway with two strands unwound of FN9 has been illustrated before in constant force simulations of FN.³³ Our model corroborates these results while providing new insight into the dynamics of FN unfolding when interacting with $\alpha_5\beta_1$ integrin.

The observed unbinding and unfolding sequence in $\alpha_5\beta_1$ -FN was not preserved at 1 nm/ns. The salt bridges, ARG1379-ASP154 and ARG1493-ASP227, simultaneously broke at 5.7 nm of extension after a short force plateau between 4.8 and 5.7 nm, but unlike in the 10 nm/ns run, FN9 did not create a new interaction with α_5



21 September 2023 16:24:44

FIG. 8. The dimensionless $\alpha_5\beta_1$ -FN bond concentration (top) and force per $\alpha_5\beta_1$ -FN (bottom) results for the baseline whole-cell simulation with $k_{int} = 1$ pN/nm. $\alpha_5\beta_1$ -FN localization and force dissipation occurred rapidly and no significant changes in distribution were observed past 6 s. Movies showing simulation trajectories can be found in the Supplementary Materials.

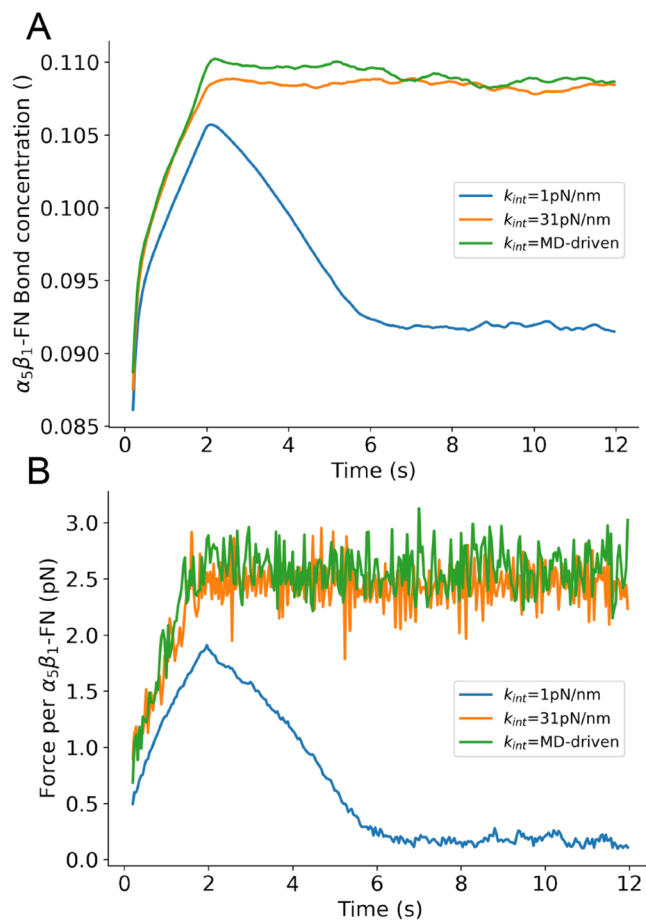


FIG. 9. Whole-cell average (a) $\alpha_5\beta_1$ -FN bond concentration (dimensionless) and (b) force per $\alpha_5\beta_1$ -FN over the simulation run. Three test conditions for $\alpha_5\beta_1$ -FN stiffness are shown per plot: (1) constant 1 pN/nm baseline from past models,^{27,28,35} (2) constant 31 pN/nm based on the first segment of the 1 nm/ns force–extension curve fit, and (3) MD-driven stiffness derived from using all segments of the curve fit.

[Fig. 7(b)]. Rather, FN10 unfolded, leading to the majority of the overall extension and reduction in force from 5.7 to 12.7 nm [Fig. 4(a)]. During FN10 unfolding, the interaction between ARG1493 in FN and ASP227 in α_5 alternated between high and low coulombic interactions while ARG1495 maintained adhesion with β_1 integrin. Due to the lack of interaction between the synergy site in FN9 and α_5 , FN9 was free to separate from integrin so FN10 could readily unfold. Once one strand had completely unfolded, due to the direction of the pulling force with respect to the orientation of FN10, the force needed to rotate FN10 prior to unwinding the second strand, which led to an increase in force [Fig. 4(b)].

At both pull rates, the synergy site and RGD loop played key roles in maintaining the adhesion between $\alpha_5\beta_1$ and FN. Specifically, the salt bridge between ARG1379 and ASP154 contributed to the molecule's initial “stiff” behavior prior to FN unfolding;

and part of the RGD loop between β_1 and FN10 was the only remaining connection between integrin and FN after full extension. Due to their instrumental role, it stands to reason that interfering with these residues via point mutations would reduce adhesion¹⁵ and rupture force.²⁰ While measured *in vitro* forces on $\alpha_5\beta_1$ -FN have been shown to be much smaller than we have presented due to our model's much faster pulling speed, nonlinear force–extension behavior, and rapid jumps in force have been observed.^{15,20,21} We showed how key residues could contribute to this characteristic behavior during $\alpha_5\beta_1$ -FN extension in a pull rate-dependent manner. To bridge the nanoscale integrin stretching to cell-scale integrin dynamics, as a proof-of-concept, we modeled the force–extension of $\alpha_5\beta_1$ as a nonlinear spring and used it to scale up to a 2D whole-cell continuum model.

C. Multiscale integration of $\alpha_5\beta_1$ -FN force–extension with whole-cell integrin dynamics

Prior to integrating the force–extension curves from the MD runs, we had run a baseline simulation of the whole-cell model with similar parameters to those commonly used in the literature.^{27,28,35} In particular, we set the $\alpha_5\beta_1$ -FN stiffness, k_{int} , to 1 pN/nm. For all simulations, the cell contractility was ramped from 0 to 200 Pa within the first 2 s and held at 200 Pa for the remainder of the 12 s simulation. Integrins were recruited to the cell border, achieving maximum concentration and force as the contractility reached 200 Pa at 2 s (Fig. 8).

Integrin's spatial distribution on the cell's leading edge during motion has been previously observed *in vitro*,²² corroborating the results from the model. During contraction, the model's average peak bond concentration reached 10.6% [Fig. 9(a)] with a max peak of 22.5%. The average force per bond followed a similar curve, reaching an average peak of 1.9 pN [Fig. 9(b)] with a max peak of 28.6 pN at the cell boundary. These bonds had short lifetimes and dissociated quickly, allowing the model to dissipate the contraction and reach equilibrium just before the 6 s mark. After reaching this equilibrium point, the mean force was 0.17 ± 0.04 pN with max forces reaching 15.9 pN at the boundary. The peak bond forces and concentrations occurred on the boundary due to the positive feedback loop of the catch-slip bond dynamics. While the strain across the cell is uniform due to the applied isotropic contractility, the deformation of the bond springs is the greatest at the boundary, leading to higher bond concentrations and forces. Overall, the forces were within the 1–38 pN range that has been observed *in vitro*^{21,36,37} and well within the peak single $\alpha_5\beta_1$ -FN rupture forces measured via AFM of 120 pN.²⁰

The baseline simulation provided a control to test against our two simulation conditions derived from the 1 nm/ns MD simulation. We defined a varying, MD-driven $\alpha_5\beta_1$ -FN stiffness as the entire 1 nm/ns force–extension curve fit. To evaluate how the nonlinearity of the MD-driven integrin spring affected whole-cell adhesion dynamics, we used the slope of the first segment, 31 pN/nm, to define a constant $\alpha_5\beta_1$ -FN stiffness test condition.

Overall, the $\alpha_5\beta_1$ -FN bond concentration for the constant and MD-driven $\alpha_5\beta_1$ -FN stiffness conditions followed a similar trend and were both slower to distribute the contraction load (Fig. 9)

21 September 2023 16:24:44

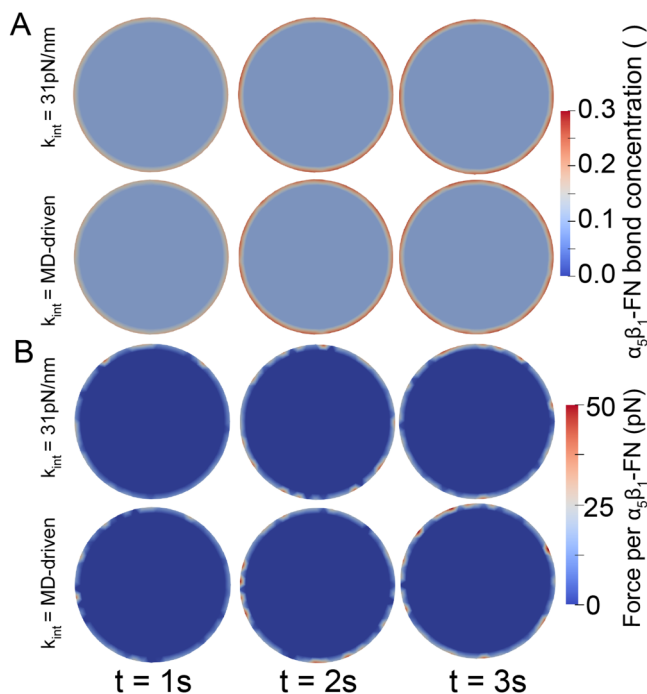


FIG. 10. Whole-cell simulation results for the constant and MD-driven spring stiffnesses. (a) $\alpha_5\beta_1$ -FN bond concentration and (b) force per $\alpha_5\beta_1$ integrin at three time frames within the first 3 s of the simulation. Dissipation continued past 3 s, but the changes were minor. Movies showing simulations can be found in the supplementary material.

than the 1 pN stiffness setting. After 2 s, the mean forces steadied at 2.45 ± 0.18 and 2.59 ± 0.19 pN for the constant and MD-driven runs, respectively. The noise in the bond concentrations and force per bond (Fig. 9) were due to the random 5 pN actin polymerization force. The results for both cases were similar. The constant 31 pN/nm run reached a max average bond concentration of 10.9% and the MD-driven case topped at 11.0%. Max average forces, located at the cell boundary (Fig. 10), were 53.5 and 55.6 pN for the 31 pN/nm and MD-driven runs, respectively. The positive feedback loop of the catch-slip bond at the boundary continued to drive the peak forces and concentrations across all stiffness settings.

Notably, model predictions surpass *in situ* rupture forces of 34–38.6 pN for $\alpha_5\beta_1$ -FN^{36,37} and 40 pN for another subtype, $\alpha_V\beta_3$.⁴⁰ Chang *et al.* used FRET-based sensors to measure adhesion forces between 1 and 7 pN on fibroblasts.²¹ Recent work has used leveraged tension gauge tethers to measure single-molecule forces on RGD-binding integrins and showed that integrin activation occurs below 12 pN and $\alpha_V\beta_1$ could sustain forces over 54 pN in mature FAs.⁴¹ In summary, the models we presented showed estimations toward the upper bounds of measured biophysical forces felt by integrin.

The MD-driven and constant 31 pN/nm integrin stiffness models showed similar force and concentration results, indicating that linear spring stiffness was sufficient to capture $\alpha_5\beta_1$ -FN molecular dynamics in this model. Notably, bond lengths were

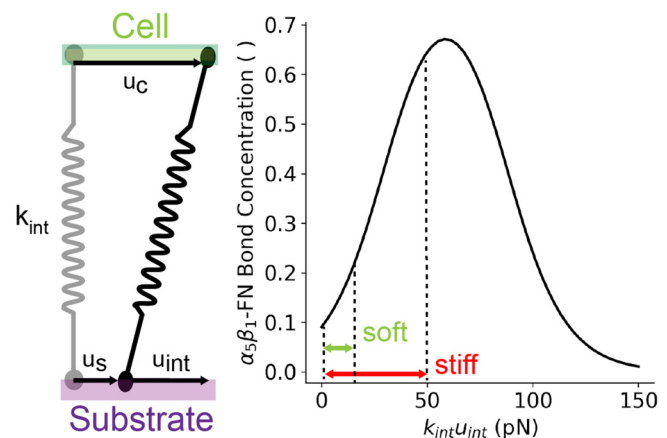


FIG. 11. Schematic of the balance at an equilibrium state between the cell, substrate, and spring deformations contribute to changing bond concentrations based on the catch-slip bond curve [Eq. (8)].

maintained below 2.5 nm, where the stiffness jumps to 99.5 pN/nm in the MD-driven force–extension curve [Fig. 4(a)]. The main difference observed in the bond force and concentration response was between soft (1 pN/nm) and stiff (31 pN/nm, MD-driven) integrin models. These differences arose due to the force balance between the cell, the substrate, the integrin, and other random forces [Eq. (13)]. All these forces contributed to the integrin deformation, u_{int} (Fig. 11), which was multiplied by integrin stiffness to calculate force. This bond concentration was updated based on this bond force and catch-slip bond model [Fig. 11 and Eq. (8)]. In our case, the bond lengths ranged from 0 to 15.9 nm for the soft integrin and 0 to 1.8 nm in the stiff integrin. This led to forces between 0 and 15.9 pN and 0 and 55.6 pN for the soft and stiff integrin, respectively. To summarize, the balance between applied forces, cell/substrate material properties, and integrin stiffness led to varying bond deformation, which contributed to alterations in bond concentration due to catch-slip bond dynamics.

IV. CONCLUSION

We developed a coupled multiscale model that showed how amino acid interactions at the synergy site in FN contribute to the nonlinear force–extension behavior of $\alpha_5\beta_1$ -FN, which leads to unique whole-cell adhesion force landscapes. The model demonstrated whole-cell integrin spatial distribution along the cell membrane, consistent with fibroblasts plated *in vitro*²² and forces within the 120 pN maximum single-molecule rupture force and 1–38 pN *in situ* rupture forces.^{21,36,37}

This study has limitations. We used high pull rates in the MD simulations to maintain reasonable computational runtimes. However, this led to large forces during $\alpha_5\beta_1$ -FN extension. While the computational cost is a common drawback of MD, the detailed data and outputs gained from the amino acid dynamics and their connection to whole-cell integrin dynamics would have been otherwise unobservable. Therefore, we believe that it was useful to

include this demanding piece of the multiscale model. A combination of slower pull rates and coarse grained MD simulations could be the compromise necessary to investigate the nonlinear mechanics while maintaining some nanoscale details.

Also, we chose $\alpha_5\beta_1$ integrin as the sole surface receptor but cells have additional subtypes with varying roles^{35,42} and potentially different adhesion strengths⁴¹ and binding kinetics.^{43,44} Given the 24 known subtypes of integrin,⁴⁵ it is critical to understand which ones are the main contributors to adhesion maintenance in the presence of specific ligands. For example, in the case of fibronectin, a recent single-cell force spectroscopy study indicated that pan integrin knockout fibroblasts only expressing $\alpha_5\beta_1$ and $\alpha_V\beta_3$ transmitted the same amount adhesive force as wildtype fibroblasts on a fibronectin coated surface.⁴⁶ Therefore, extending our model to contain these two subtypes may be an appropriate approximation to evaluate integrin adhesion mechanics for fibroblasts on fibronectin. Another key consideration is the dynamics of low-affinity and high-affinity conformations of integrin. For our model, we assumed that $\alpha_5\beta_1$ integrin was in a high-affinity, extended-open conformation. However, it has been demonstrated that low-affinity bent-closed and extended-closed conformations of $\alpha_5\beta_1$ and $\alpha_V\beta_3$ can still bind to fibronectin.^{44,47} To include the contributions of varying subtypes, it would be necessary to update to our catch-slip bond model (Fig. 11) to include high and low-affinity conformational states, manage the population distribution of integrin subtypes as done in other models,^{28,35} and expand on existing steered MD characterizations of $\alpha_V\beta_3$ ^{30,48} to add to ours of $\alpha_5\beta_1$. Overall, more investigation is needed to evaluate how integrin subtypes collaborate to manage cell adhesion dynamics.

The model assumed a homogeneous substrate. However, tissue microenvironments are spatially heterogeneous and respond to the binding and unbinding dynamics between extracellular matrix (ECM) fibers.^{49–53} This leads to viscoplastic material behavior, or time and frequency dependent force dissipation,⁵⁴ which mediates cell migration, differentiation, and disease progression.^{55–57} To include these effects, we could represent the substrate viscoplasticity via the Norton–Hoff constitutive model,^{49,58} and the cell's myosin-actin engagement via the molecular or motor clutch model.^{53,59} We would expect a heterogeneity to arise in the force and spatial distribution of the integrin bonds, localizing near denser packs of crosslinked fibers. We hypothesize that stiffer integrins would lead to denser packing of ECM fibers due to their slow rate of sustained force compared to softer bonds. However, more investigation is needed to reveal the relationship between cell adhesion and force-mediated ECM fiber mechanics.

Our model focused on cell adhesion mechanics and has the potential to grow into a framework that can investigate cell mechanotransduction across multiple scales. For example, we could test how unique mutations on integrins affect whole-cell dynamics *in silico*. Additionally, by incorporating the cell nucleus, we could support early evidence to show how its mechanosensitive nature and material properties could govern gene transcription.^{60–62} Key components that have previously been modeled, such as the cell membrane, integrin's transmembrane domain, and integrin clustering and diffusion^{28,35,63–65} were omitted from our model for simplicity but could be added as new multiscale mechanobiological questions are posed regarding their mechanics. Last, our multiscale

framework could be broadened to reveal the nano- and micro-mechanics within nascent engineered tissues and organ-chips that apply controllable biophysical loads at the cell membrane.^{66–71}

SUPPLEMENTARY MATERIAL

See the supplementary material for detailed equations and parameters for the whole-cell model; parameters for the minimization, equilibration, and force distribution analysis of the MD model; RMSD, pressure, and temperature during equilibration; whole-cell model mesh and timestep convergence studies; and trajectory movies for the whole-cell and MD models. The whole-cell model is available at <https://github.com/dredremontes/wholeCellFE> and the MD model is available at https://github.com/dredremontes/pull_integrinMD.

ACKNOWLEDGMENTS

This research used Stampede2 at Texas Advanced Computing Center through allocation MCB100146 from Advanced Cyberinfrastructure Coordination Ecosystem: Services & Support (ACCESS) super-computing facilities, supported by the National Science Foundation (NSF) (Grant Nos. 2138259, 2138286, 2138307, 2137603, and 2138296). A.R.M. was funded by the Ford Foundation's Predoctoral Fellowship awarded by the National Academies of Science, Engineering, and Medicine and the Robert N. Noyce Fellowship from UC Berkeley's College of Engineering. G.G. was supported by the National Science Foundation California Alliance for Minority Participation. Thank you to Ghafar Yerima and Nya Domkam for helping set up GROMACS and gromacs-fda. We also thank the Molecular Cell Biomechanics Lab and the Berkeley Biomechanics Lab for fruitful discussions that improved the manuscript. This work was supported in part by the Miller Institute for Basic Research in Science through the Visiting Professor fellowship to A.B.T.

AUTHOR DECLARATIONS

Conflict of Interest

The authors have no conflicts to disclose.

Author Contributions

Andre R. Montes: Conceptualization (equal); Data curation (equal); Formal analysis (equal); Funding acquisition (equal); Investigation (equal); Methodology (equal); Project administration (equal); Software (equal); Validation (equal); Visualization (equal); Writing – original draft (equal); Writing – review & editing (equal). **Gabriela Gutierrez:** Formal analysis (supporting); Investigation (equal). **Adrian Buganza Tepole:** Conceptualization (equal); Data curation (equal); Formal analysis (equal); Funding acquisition (equal); Investigation (equal); Methodology (equal); Project administration (equal); Resources (equal); Software (equal); Supervision (equal); Validation (equal); Visualization (equal); Writing – original draft (equal); Writing – review & editing (equal). **Mohammad R. K. Mofrad:** Conceptualization (equal); Funding acquisition (equal); Resources (equal); Supervision (equal); Writing – review & editing (equal).

DATA AVAILABILITY

The data that support the findings of this study are available from the corresponding author upon reasonable request.

REFERENCES

- ¹D. E. Ingber, "Mechanosensation through integrins: Cells act locally but think globally," *Proc. Natl. Acad. Sci. U.S.A.* **100**, 1472–1474 (2003).
- ²Z. Jahed, H. Shams, M. Mehrbod, and M. R. Mofrad, "Mechanotransduction pathways linking the extracellular matrix to the nucleus," *Int. Rev. Cell Mol. Biol.* **310**, 171–220 (2014).
- ³J. Zhu, C. V. Carman, M. Kim, M. Shimaoka, T. A. Springer, and B.-H. Luo, "Requirement of α and β subunit transmembrane helix separation for integrin outside-in signaling," *Blood* **110**, 2475–2483 (2007).
- ⁴P. E. Hughes, F. Diaz-Gonzalez, L. Leong, C. Wu, J. A. McDonald, S. J. Shattil, and M. H. Ginsberg, "Breaking the integrin hinge: A defined structural constraint regulates integrin signaling," *J. Biol. Chem.* **271**, 6571–6574 (1996).
- ⁵E. Puklin-Faucher and M. P. Sheetz, "The mechanical integrin cycle," *J. Cell Sci.* **122**, 179–186 (2009).
- ⁶J. Takagi, B. M. Petre, T. Walz, and T. A. Springer, "Global conformational rearrangements in integrin extracellular domains in outside-in and inside-out signaling," *Cell* **110**, 599–611 (2002).
- ⁷S. W. Moore, P. Roca-Cusachs, and M. P. Sheetz, "Stretchy proteins on stretchy substrates: The important elements of integrin-mediated rigidity sensing," *Dev. Cell* **19**, 194–206 (2010).
- ⁸J. Deng, C. Zhao, J. P. Spatz, and Q. Wei, "Nanopatterned adhesive, stretchable hydrogel to control ligand spacing and regulate cell spreading and migration," *ACS Nano* **11**, 8282–8291 (2017).
- ⁹J. Lee, A. A. Abdeen, D. Zhang, and K. A. Kilian, "Directing stem cell fate on hydrogel substrates by controlling cell geometry, matrix mechanics and adhesion ligand composition," *Biomaterials* **34**, 8140–8148 (2013).
- ¹⁰P. Moreno-Layseca, J. Icha, H. Hamidi, and J. Ivaska, "Integrin trafficking in cells and tissues," *Nat. Cell Biol.* **21**, 122–132 (2019).
- ¹¹J. Takagi, K. Strokovich, T. A. Springer, and T. Walz, "Structure of integrin $\alpha 5 \beta 1$ in complex with fibronectin," *EMBO J.* **22**, 4607–4615 (2003).
- ¹²S. Schumacher, D. Dedden, R. V. Nunez, K. Matoba, J. Takagi, C. Biertümpfel, and N. Mizuno, "Structural insights into integrin $\alpha 5 \beta 1$ opening by fibronectin ligand," *Sci. Adv.* **7**, eabe9716 (2021).
- ¹³T. Nagai, N. Yamakawa, S.-I. Aota, S. S. Yamada, S. K. Akiyama, K. Olden, and K. M. Yamada, "Monoclonal antibody characterization of two distant sites required for function of the central cell-binding domain of fibronectin in cell adhesion, cell migration, and matrix assembly," *J. Cell Biol.* **114**, 1295–1305 (1991).
- ¹⁴I. Wierzbicka-Patynowski and J. E. Schwarzbauer, "The ins and outs of fibronectin matrix assembly," *J. Cell Sci.* **116**, 3269–3276 (2003).
- ¹⁵J. C. Friedland, M. H. Lee, and D. Boettiger, "Mechanically activated integrin switch controls $\alpha 5 \beta 1$ function," *Science* **323**, 642–644 (2009).
- ¹⁶D. Barkan, L. H. El Touny, A. M. Michalowski, J. A. Smith, I. Chu, A. S. Davis, J. D. Webster, S. Hoover, R. M. Simpson, J. Gaudie, and J. E. Green, "Metastatic growth from dormant cells induced by a col-I-enriched fibrotic environment metastatic outgrowth from dormant tumor cells," *Cancer Res.* **70**, 5706–5716 (2010).
- ¹⁷J. Z. Kechagia, J. Ivaska, and P. Roca-Cusachs, "Integrins as biomechanical sensors of the microenvironment," *Nat. Rev. Mol. Cell Biol.* **20**, 457–473 (2019).
- ¹⁸M. J. Paszek, N. Zahir, K. R. Johnson, J. N. Lakins, G. I. Rozenberg, A. Gefen, C. A. Reinhart-King, S. S. Margulies, M. Dembo, D. Boettiger, D. A. Hammer, and V. M. Weaver, "Tensional homeostasis and the malignant phenotype," *Cancer Cell* **8**, 241–254 (2005).
- ¹⁹J. J. Northey, L. Przybyla, and V. M. Weaver, "Tissue force programs cell fate and tumor aggression mechanotransduction in cell fate and cancer aggression," *Cancer Discovery* **7**, 1224–1237 (2017).
- ²⁰F. Li, S. D. Redick, H. P. Erickson, and V. T. Moy, "Force measurements of the $\alpha 5 \beta 1$ integrin–fibronectin interaction," *Biophys. J.* **84**, 1252–1262 (2003).
- ²¹A. C. Chang, A. H. Mekhdjian, M. Morimatsu, A. K. Denisin, B. L. Pruitt, and A. R. Dunn, "Single molecule force measurements in living cells reveal a minimally tensioned integrin state," *ACS Nano* **10**, 10745–10752 (2016).
- ²²M. Benito-Jardon, S. Klapproth, I. Gimeno-LLuch, T. Petzold, M. Bharadwaj, D. J. Müller, G. Zuchtriegel, C. A. Reichel, and M. Costell, "The fibronectin synergy site re-enforces cell adhesion and mediates a crosstalk between integrin classes," *eLife* **6**, e22264 (2017).
- ²³L. Schrödinger, "The PyMOL molecular graphics system, version 1.8" (2015).
- ²⁴M. J. Abraham, T. Murtola, R. Schulz, S. Páll, J. C. Smith, B. Hess, and E. Lindahl, "Gromacs: High performance molecular simulations through multi-level parallelism from laptops to supercomputers," *SoftwareX* **1**, 19–25 (2015).
- ²⁵W. Humphrey, A. Dalke, and K. Schulten, "VMD—Visual molecular dynamics," *J. Mol. Graph.* **14**, 33–38 (1996).
- ²⁶L. Treloar, "The elasticity and related properties of rubbers," *Rep. Prog. Phys.* **36**, 755 (1973).
- ²⁷Y. Guo, S. Calve, and A. B. Tepole, "Multiscale mechanobiology: Coupling models of adhesion kinetics and nonlinear tissue mechanics," *Biophys. J.* **121**, 525–539 (2022).
- ²⁸B. Cheng, W. Wan, G. Huang, Y. Li, G. M. Genin, M. R. Mofrad, T. J. Lu, F. Xu, and M. Lin, "Nanoscale integrin cluster dynamics controls cellular mechanosensing via FAKY397 phosphorylation," *Sci. Adv.* **6**, eaax1909 (2020).
- ²⁹T. Brochu and R. Bridson, "Robust topological operations for dynamic explicit surfaces," *SIAM J. Comput.* **31**, 2472–2493 (2009).
- ³⁰W. Chen, J. Lou, J. Hsin, K. Schulten, S. C. Harvey, and C. Zhu, "Molecular dynamics simulations of forced unbending of integrin $\alpha v \beta 3$," *PLoS Comput. Biol.* **7**, e1001086 (2011).
- ³¹M. Kulke and W. Langel, "Molecular dynamics simulations to the bidirectional adhesion signaling pathway of integrin $\alpha v \beta 3$," *Proteins: Struct. Funct. Bioinform.* **88**, 679–688 (2020).
- ³²F. Kong, A. J. García, A. P. Mould, M. J. Humphries, and C. Zhu, "Demonstration of catch bonds between an integrin and its ligand," *J. Cell Biol.* **185**, 1275–1284 (2009).
- ³³M. Gao, D. Craig, V. Vogel, and K. Schulten, "Identifying unfolding intermediates of FN-III10 by steered molecular dynamics," *J. Mol. Biol.* **323**, 939–950 (2002).
- ³⁴A. R. Bausch, F. Ziemann, A. A. Boulbitch, K. Jacobson, and E. Sackmann, "Local measurements of viscoelastic parameters of adherent cell surfaces by magnetic bead microrheometry," *Biophys. J.* **75**, 2038–2049 (1998).
- ³⁵T. C. Bidone, A. V. Skeeters, P. W. Oakes, and G. A. Voth, "Multiscale model of integrin adhesion assembly," *PLoS Comput. Biol.* **15**, e1007077 (2019).
- ³⁶A. Trache, J. P. Trzeciakowski, L. Gardiner, Z. Sun, M. Muthuchamy, M. Guo, S. Y. Yuan, and G. A. Meininger, "Histamine effects on endothelial cell fibronectin interaction studied by atomic force microscopy," *Biophys. J.* **89**, 2888–2898 (2005).
- ³⁷X. Wu, Z. Sun, A. Foskett, J. P. Trzeciakowski, G. A. Meininger, and M. Muthuchamy, "Cardiomyocyte contractile status is associated with differences in fibronectin and integrin interactions," *Am. J. Physiol.* **298**, H2071–H2081 (2010).
- ³⁸P. Roca-Cusachs, T. Iskratsch, and M. P. Sheetz, "Finding the weakest link—Exploring integrin-mediated mechanical molecular pathways," *J. Cell Sci.* **125**, 3025–3038 (2012).
- ³⁹A. F. Oberhauser, C. Badilla-Fernandez, M. Carrion-Vazquez, and J. M. Fernandez, "The mechanical hierarchies of fibronectin observed with single-molecule AFM," *J. Mol. Biol.* **319**, 433–447 (2002).
- ⁴⁰X. Wang and T. Ha, "Defining single molecular forces required to activate integrin and notch signaling," *Science* **340**, 991–994 (2013).
- ⁴¹M. H. Jo, J. Li, V. Jaumouillé, Y. Hao, J. Coppola, J. Yan, C. M. Waterman, T. A. Springer, and T. Ha, "Single-molecule characterization of subtype-specific $\beta 1$ integrin mechanics," *Nat. Commun.* **13**, 7471 (2022).
- ⁴²J. L. Young, X. Hua, H. Somsel, F. Reichart, H. Kessler, and J. P. Spatz, "Integrin subtypes and nanoscale ligand presentation influence drug sensitivity in cancer cells," *Nano Lett.* **20**, 1183–1191 (2020).

- ⁴³P. Kanchanawong and D. A. Calderwood, "Organization, dynamics and mechanoregulation of integrin-mediated cell-ECM adhesions," *Nat. Rev. Mol. Cell Biol.* **24**, 142–161 (2023).
- ⁴⁴J. Li, J. Yan, and T. A. Springer, "Low-affinity integrin states have faster ligand-binding kinetics than the high-affinity state," *eLife* **10**, e73359 (2021).
- ⁴⁵Y. Takada, X. Ye, and S. Simon, "The integrins," *Genome Biol.* **8**, 1–9 (2007).
- ⁴⁶N. Strohmeyer, M. Bharadwaj, M. Costell, R. Fässler, and D. J. Müller, "Fibronectin-bound $\alpha_5\beta_1$ integrins sense load and signal to reinforce adhesion in less than a second," *Nat. Mater.* **16**, 1262–1270 (2017).
- ⁴⁷Y. Chen, H. Lee, H. Tong, M. Schwartz, and C. Zhu, "Force regulated conformational change of integrin $\alpha_v\beta_3$," *Matrix Biol.* **60**, 70–85 (2017).
- ⁴⁸N. Li, S. Qiu, Y. Fang, J. Wu, and Q. Li, "Comparison of linear vs cyclic RGD pentapeptide interactions with integrin $\alpha_v\beta_3$ by molecular dynamics simulations," *Biology* **10**, 688 (2021).
- ⁴⁹A. Malandrino, X. Trepap, R. D. Kamm, and M. Mak, "Dynamic filopodial forces induce accumulation, damage, and plastic remodeling of 3D extracellular matrices," *PLoS Comput. Biol.* **15**, e1006684 (2019).
- ⁵⁰O. Chaudhuri, J. Cooper-White, P. A. Janmey, D. J. Mooney, and V. B. Shenoy, "Effects of extracellular matrix viscoelasticity on cellular behaviour," *Nature* **584**, 535–546 (2020).
- ⁵¹S. Münster, L. M. Jawerth, B. A. Leslie, J. I. Weitz, B. Fabry, and D. A. Weitz, "Strain history dependence of the nonlinear stress response of fibrin and collagen networks," *Proc. Natl. Acad. Sci. U.S.A.* **110**, 12197–12202 (2013).
- ⁵²C. Liu, R. Y. Nguyen, G. A. Pizzurro, X. Zhang, X. Gong, A. R. Martinez, and M. Mak, "Self-assembly of mesoscale collagen architectures and applications in 3D cell migration," *Acta Biomater.* **155**, 167–181 (2023).
- ⁵³A. Elosegui-Artola, "The extracellular matrix viscoelasticity as a regulator of cell and tissue dynamics," *Curr. Opin. Cell Biol.* **72**, 10–18 (2021).
- ⁵⁴P. Sacco, F. Piazza, C. Pizzolitto, G. Baj, F. Brun, E. Marsich, and I. Donati, "Regulation of substrate dissipation via tunable linear elasticity controls cell activity," *Adv. Funct. Mater.* **32**, 2200309 (2022).
- ⁵⁵Y. Ma, T. Han, Q. Yang, J. Wang, B. Feng, Y. Jia, Z. Wei, and F. Xu, "Viscoelastic cell microenvironment: Hydrogel-based strategy for recapitulating dynamic ECM mechanics," *Adv. Funct. Mater.* **31**, 2100848 (2021).
- ⁵⁶W. Li, D. Wu, D. Hu, S. Zhu, C. Pan, Y. Jiao, L. Li, B. Luo, C. Zhou, and L. Lu, "Stress-relaxing double-network hydrogel for chondrogenic differentiation of stem cells," *Mater. Sci. Eng. C* **107**, 110333 (2020).
- ⁵⁷R. Y. Nguyen, A. T. Cabral, A. Rossello-Martinez, A. Zulli, X. Gong, Q. Zhang, J. Yan, and M. Mak, "Tunable mesoscopic collagen island architectures modulate stem cell behavior," *Adv. Mater.* **35**, 2207882 (2023).
- ⁵⁸N. J. Hoff, "Approximate analysis of structures in the presence of moderately large creep deformations," *Q. Appl. Math.* **12**, 49–55 (1954).
- ⁵⁹Z. Gong, S. E. Szczesny, S. R. Caliri, E. E. Charrier, O. Chaudhuri, X. Cao, Y. Lin, R. L. Mauck, P. A. Janmey, J. A. Burdick, and V. B. Shenoy, "Matching material and cellular timescales maximizes cell spreading on viscoelastic substrates," *Proc. Natl. Acad. Sci. U.S.A.* **115**, E2686–E2695 (2018).
- ⁶⁰N. Wang, J. D. Tytell, and D. E. Ingber, "Mechanotransduction at a distance: Mechanically coupling the extracellular matrix with the nucleus," *Nat. Rev. Mol. Cell Biol.* **10**, 75–82 (2009).
- ⁶¹S. Wang, E. Stoops, U. Cp, B. Markus, A. Reuveny, E. Ordan, and T. Volk, "Mechanotransduction via the LINC complex regulates DNA replication in myonuclei," *J. Cell Biol.* **217**, 2005–2018 (2018).
- ⁶²S. Tsukamoto, T. Asakawa, S. Kimura, N. Takesue, M. R. Mofrad, and N. Sakamoto, "Intranuclear strain in living cells subjected to substrate stretching: A combined experimental and computational study," *J. Biomech.* **119**, 110292 (2021).
- ⁶³M. J. Paszek, D. Boettiger, V. M. Weaver, and D. A. Hammer, "Integrin clustering is driven by mechanical resistance from the glycocalyx and the substrate," *PLoS Comput. Biol.* **5**, e1000604 (2009).
- ⁶⁴M. Mehrbod and M. R. Mofrad, "Localized lipid packing of transmembrane domains impedes integrin clustering," *PLoS Comput. Biol.* **9**, e1002948 (2013).
- ⁶⁵M. Mehrbod, S. Trisno, and M. R. Mofrad, "On the activation of integrin $\alpha IIb\beta_3$: Outside-in and inside-out pathways," *Biophys. J.* **105**, 1304–1315 (2013).
- ⁶⁶A. Elosegui-Artola, A. Gupta, A. J. Najibi, B. R. Seo, R. Garry, C. M. Tringides, I. de Lázaro, M. Darnell, W. Gu, Q. Zhou *et al.*, "Matrix viscoelasticity controls spatiotemporal tissue organization," *Nat. Mater.* **22**, 1–11 (2022).
- ⁶⁷G. R. López-Marcial, A. Y. Zeng, C. Osuna, J. Dennis, J. M. García, and G. D. O'Connell, "Agarose-based hydrogels as suitable bioprinting materials for tissue engineering," *ACS Biomater. Sci. Eng.* **4**, 3610–3616 (2018).
- ⁶⁸J. P. McKinley, A. R. Montes, M. N. Wang, A. R. Kamath, G. Jimenez, J. Lim, S. A. Marathe, M. R. Mofrad, and G. D. O'Connell, "Design of a flexing organ-chip to model in situ loading of the intervertebral disc," *Biomicrofluidics* **16**, 054111 (2022).
- ⁶⁹J. E. Barthold, B. M. St. Martin, S. L. Sridhar, F. Vernerey, S. E. Schneider, A. Wacquez, V. L. Ferguson, S. Calve, and C. P. Neu, "Recellularization and integration of dense extracellular matrix by percolation of tissue microparticles," *Adv. Funct. Mater.* **31**, 2103355 (2021).
- ⁷⁰P. Dhavalikar, A. Robinson, Z. Lan, D. Jenkins, M. Chwatko, K. Salhadar, A. Jose, R. Kar, E. Shoga, A. Kannapiran, and E. Cosgriff-Hernandez, "Review of integrin-targeting biomaterials in tissue engineering," *Adv. Healthcare Mater.* **9**, 2000795 (2020).
- ⁷¹A. Sontheimer-Phelps, B. A. Hassell, and D. E. Ingber, "Modelling cancer in microfluidic human organs-on-chips," *Nat. Rev. Cancer* **19**, 65–81 (2019).